








Cite this: *Lab Chip*, 2021, 21, 2932

Sample-to-answer COVID-19 nucleic acid testing using a low-cost centrifugal microfluidic platform with bead-based signal enhancement and smartphone read-out†

Ruben R. G. Soares, ^a Ahmad S. Akhtar, ^a Inês F. Pinto, ^a Noa Lapins,^a Donal Barrett,^b Gustaf Sandh,^c Xiushan Yin,^{bde} Vicent Pelechano ^b and Aman Russom ^{*af}

With its origin estimated around December 2019 in Wuhan, China, the ongoing SARS-CoV-2 pandemic is a major global health challenge. The demand for scalable, rapid and sensitive viral diagnostics is thus particularly pressing at present to help contain the rapid spread of infection and prevent overwhelming the capacity of health systems. While high-income countries have managed to rapidly expand diagnostic capacities, such is not the case in resource-limited settings of low- to medium-income countries. Aiming at developing cost-effective viral load detection systems for point-of-care COVID-19 diagnostics in resource-limited and resource-rich settings alike, we report the development of an integrated modular centrifugal microfluidic platform to perform loop-mediated isothermal amplification (LAMP) of viral RNA directly from heat-inactivated nasopharyngeal swab samples. The discs were pre-packed with dried *n*-benzyl-*n*-methylethanolamine modified agarose beads used to selectively remove primer dimers, inactivate the reaction post-amplification and allowing enhanced fluorescence detection *via* a smartphone camera. Sample-to-answer analysis within 1 hour from sample collection and a detection limit of approximately 100 RNA copies in 10 μ L reaction volume were achieved. The platform was validated with a panel of 162 nasopharyngeal swab samples collected from patients with COVID-19 symptoms, providing a sensitivity of 96.6% (82.2–99.9%, 95% CI) for samples with Ct values below 26 and a specificity of 100% (90–100%, 95% CI), thus being fit-for-purpose to diagnose patients with a high risk of viral transmission. These results show significant promise towards bringing routine point-of-care COVID-19 diagnostics to resource-limited settings.

Received 29th March 2021,
Accepted 7th June 2021

DOI: 10.1039/d1lc00266j

rsc.li/loc

1. Introduction

Simple, rapid, and sensitive analytical methods for viral detection at the point-of-care have been increasingly in demand in recent decades. Such devices are especially

relevant in resource-limited settings (RLS) in Africa, Asia and South America, where the prevalence of ubiquitous viral pathogens such as human immunodeficiency virus (HIV) and other tropical viruses including Zika, Ebola, Crimean-Congo hemorrhagic fever (CCHF), chikungunya and dengue claim tens of thousands of human lives per year mostly due to the lack of effective diagnostics and subsequent disease containment and therapy.^{1–3} However, few occasions in modern history have been more pressing for developments in this field than the present SARS-CoV-2 coronavirus pandemic⁴ which from December 2019 to May 2021 has infected more than 160 million people in over 210 countries and territories, resulting in more than 3.3 million deaths.

The first cases of SARS-CoV-2 infection were reported in December 2019 in Wuhan with a probable zoonotic origin considering its genome sequence is closely related to bat coronaviruses.⁵ Although other human coronaviruses associated with epidemic outbreaks, *i.e.* SARS-CoV and

^a KTH Royal Institute of Technology, Division of Nanobiotechnology, Department of Protein Science, Science for Life Laboratory, Solna, Sweden. E-mail: aman@kth.se

^b Science for Life Laboratory, Department of Microbiology, Tumor and Cell Biology, Karolinska Institutet, Solna, Sweden

^c Department of Clinical Microbiology, Karolinska University Hospital, Stockholm, Sweden

^d Applied Biology Laboratory, Shenyang University of Chemical Technology, Shenyang, China

^e Biotech and Biomedicine Science Co. Ltd, Shenyang, China

^f AIMES – Center for the Advancement of Integrated Medical and Engineering Sciences at Karolinska Institutet and, KTH Royal Institute of Technology, Stockholm, Sweden

† Electronic supplementary information (ESI) available. See DOI: 10.1039/d1lc00266j



Concerning the development of portable analytical devices, the use of RT-PCR is suboptimal considering the

Here, LAMP, centrifugal microfluidics, smartphone-based detection and recent developments in RT-LAMP applied to the detection of SARS-CoV-2 RNA^{34–40} are combined to develop a novel cost-effective and fully integrated platform for COVID-19 diagnostics directly from heat-inactivated nasopharyngeal samples. The direct detection from heat-inactivated samples was achieved using (1) a one-pot combination of reverse transcriptase and polymerase enzymes for robust isothermal amplification and (2) an agarose bead-based signal enhancement strategy for improved fluorometric detection, thus avoiding the impact of collection media on weakly-buffered pH responsive colorimetric amplification mixtures.⁴⁰ This signal enhancement strategy relies on a previously unreported molecular size-selectivity of *N*-benzyl-*N*-methylethanolamine (NBNM) agarose beads, trade named Capto adhere, allowing the separation of short single stranded primer oligos and large double stranded LAMP amplification products.

2. Methods

2.1. Fabrication of PDMS microchannels and discs

The PDMS microchannels used for fluorescence microscopy characterization were fabricated as described in detail elsewhere.⁴¹ Briefly, microchannels comprising a $700 \times 100 \mu\text{m}^2$ cross section converging into a $200 \times 20 \mu\text{m}^2$ cross-section aimed at trapping agarose beads with an average diameter of $90 \mu\text{m}$, were fabricated using standard SU-8 mold replication techniques. 18-Gauge inlet and outlet access holes were punched using a blunt syringe and the channels were sealed against Corning glass slides after an oxygen plasma treatment (30 s, Femto Science CUTE, 100 W, 80 Pa O_2).

The discs were designed using Autodesk® Fusion 360 (education license) and cut into 1 mm thick PMMA sheets using computer-numerical-control milling machine (Roland Model A MDX-40A). The disc layers were bonded together using clear medical grade pressure-sensitive adhesive (PSA) (ARcare® 92712). The microchannels on the PSA were cut using a cutter plotter (Graphtec CE6000-40). After aligning the PMMA layers with the PSA layer, the disc was placed in a manual press machine overnight to ensure uniform bonding. Detailed dimensions of each microchannel are shown in Fig. S3.†

2.2. Assembly of the heating module

The heating module consisted of two silicone heater mats (30 W, $150 \times 200 \text{ mm}$, 12 V DC; RS PRO Article # 731-366) which were used to heat up 1 mm thick copper plates (120 mm diameter). The heater mats are self-adhesive and the copper plates were attached to the mats. A 4 mm thick PMMA sheet served as a chamber for the heating module, having a slot, made with a CNC milling machine, to insert the disc. Heater mats with the attached copper plates in the center were attached on either side of the PMMA sheet, thus forming a heating chamber for the disc with an open slit on the side for inserting disc. The thickness of the copper plates and PMMA sheets was chosen to ensure direct contact with the two copper plates upon insertion of the disc into the chamber. Finally, the heating chamber was closed to ensure rapid and uniform heating using a PMMA part cut to fit into the slit opening. The heating module was lined with insulating foam on either side and placed between two 4 mm thick PMMA sheets ($150 \times 250 \text{ mm}$) which were then closed using M6 bolts on the 4 corners. A thermocouple (Type K; RS PRO Article # 621-2170) was embedded between the copper plate and the heater mat to measure the temperature. Temperature regulation was achieved by using N-channel MOSFET (IRF540PBF, 28A, 100 V; RS PRO Article # 708-5143) in combination with Arduino UNO Rev 3 MCU development board controlling the power supply to the heater mats.

2.3. Assembly of the centrifugal and signal acquisition modules

The centrifugal module ($140 \times 230 \times 80 \text{ mm}$) was fabricated using 4 mm thick PMMA sheets which were cut using CNC

milling machine and assembled using M3 bolts and nuts. It consisted of two chambers; the bottom chamber served as the housing for the electronic components and the top chamber is where the rotation of the disc and the signal acquisition was done. The control of the whole platform is achieved using an Arduino UNO Rev 3 MCU development board. In the center of the top chamber there was a motor (Emax MT-2204; 2300 kv brushless DC motor) used to rotate the disc. A small piece of magnetic tape was attached to the body of the motor and a bipolar hall effect sensor (Honeywell SS411A; RS Pro Article # 181-1463) was used to measure the rotation speed in real time while sending feedback to the Arduino board. The top chamber also included a blue laser diode (Osram Opto PL 450 nm, 80 mW; RS PRO Article # 758-7810) which was used for signal acquisition. A 16×2 pixel display module attached at the front provides information to the user regarding ongoing assay steps. Further technical details and exploded view is shown in Fig. S4.†

2.4. Packing, drying and characterization of *N*-benzyl-*N*-methylethanolamine (NBNM) agarose beads

The NBNM agarose beads were packed in the discs by first diluting the bead resin stock (Capto Adhere, Cytiva) in DI-water at 10% (v/v). $20 \mu\text{L}$ of the diluted bead stock were then added to each channel on the disc and subsequently centrifuged at 6000 rpm for 10 s. The excess solution was manually removed from the outlet and the disc was subsequently placed in a vacuum chamber at 15 Pa for 8 min to dehydrate the beads. After dehydration, the disc was centrifuged a second time at 6000 rpm for 10 s to ensure a homogeneous packing. The bp-cutoff of the beads packed inside the discs was characterized by microfluidic capillary electrophoresis in a Bioanalyzer 2100 system with a DNA 1000 kit (Agilent Technologies, USA).

The packing in the PDMS microchannels was performed by first preparing a suspension of beads in a 20% PEG 8000 (w/w) solution by adding $1 \mu\text{L}$ bead stock to $19 \mu\text{L}$ PEG solution. The suspension was flowed into the microchannels at $10 \mu\text{L min}^{-1}$ using a NE-1200 syringe pump (New Era Pump Systems, USA). The channels were then rinsed with DI-water flowed at $10 \mu\text{L min}^{-1}$ for 5 min to ensure removal of any residual PEG and salts. To dehydrate the beads, the PDMS device was placed in a vacuum chamber at 15 Pa for 5 min and subsequently stored at room temperature until further usage. The beads inside the PDMS devices were characterized by fluorescence microscopy in a Nikon Ti-Eclipse inverted microscope equipped with a Lumencor SOLA light engine and a FITC filter cube. The acquired fluorescence microscopy images were analyzed using ImageJ software (NIH, USA).

2.5. Real-time loop mediated isothermal amplification (RT-LAMP) of SARS-CoV-2 RNA

The RT-LAMP was performed in a Mic qPCR cycler (Biomolecular systems, Australia) with a total of $10 \mu\text{L}$ per



Lab Chip, 2021, **21**, 2932–2944 | 2935

fluorescence signal.⁴⁵ This non-specific signal is particularly relevant at room temperature due to the lower hybridization stringency, hindering a simple, non-real-time, post-LAMP measurement.⁴⁶ Several approaches have been developed to overcome this limitation involving sequence specific detection of LAMP products in a homogeneous manner, such as detection of amplification by release of quenching (DARQ), quenching of unincorporated amplification signal reporters (QUASR) and one-step strand displacement (OSD).⁴⁷ However, all of these methods imply additional specific oligos and their modification with organic fluorophores and quenchers, significantly increasing efforts in assay design and intrinsic costs per test. As a specific example, considering a typical

fluorophore-quencher hairpin probe used as a molecular beacon at a concentration of 200 nM per 10 μ L reaction volume, its cost for 100 tests would be \sim 1.2 USD, whereas SYBR Green I dye at 1 \times concentration costs less than 0.02 USD, a 60-fold reduction.

Here, to strike an innovative compromise between fit-for-purpose performance and cost-effectiveness, the developed device incorporates an agarose bead-based strategy combined with centrifugal microfluidics to fundamentally tackle these limitations and significantly enhance the negative-to-positive signal ratio at room-temperature. Using a set of primers that we have previously developed³⁴ (referred below as iLACO primer set) and resorting to a combination of SSIV and Bst

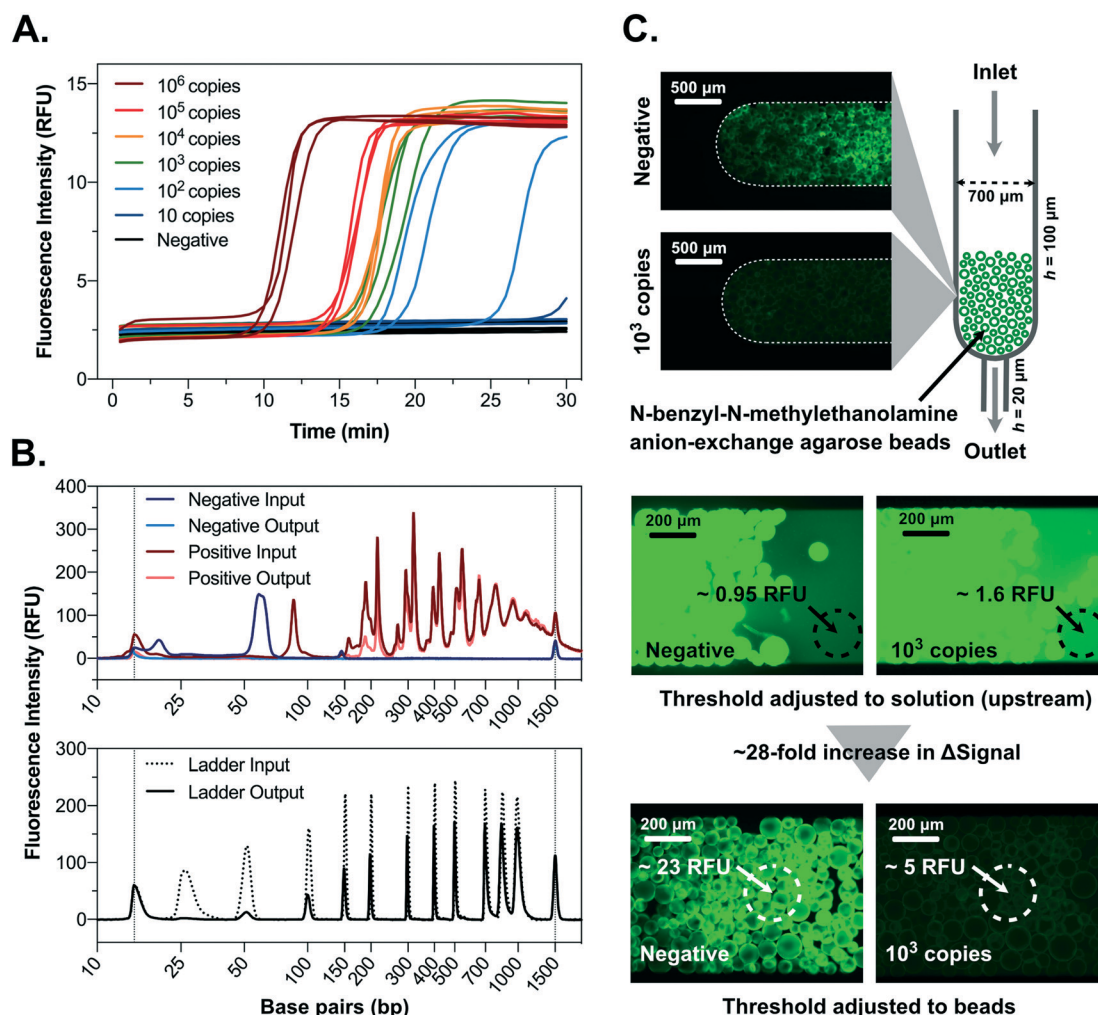


Fig. 1 Characterization of LAMP assay and bead-based signal enhancement. A – Dilution series of SARS-CoV-2 RNA fragment spiked in water. The RNA copies were added to a 10 μ L reaction mix and measured in triplicate. B (top) – Capillary electropherograms of the LAMP master mixes incubated at 65 $^{\circ}$ C for 30 min in the presence (positive) or absence (negative) of 10⁶ SARS-CoV-2 RNA fragment copies before (input) and after (output) processing using NBNM beads packed on a disc. B (bottom) – Capillary electropherogram of a DNA ladder (25–1000 bp) before (input) and after (output) processing using NBNM beads packed on a disc. Peaks below and above 25 and 1000 bp, respectively, correspond to the boundaries of the electropherogram. C – Fluorescence microscopy of NBNM beads packed on a PDMS microcolumn after flowing a LAMP mixture pre-incubated at 65 $^{\circ}$ C for 30 min in the presence (positive) or absence (negative) of 10³ SARS-CoV-2 RNA fragment copies. The signals were measured at room temperature as average grayscale intensities on the highlighted regions. Δ Signal refers to the difference in signal magnitude between the positive and negative sample measured on the solution upstream of the beads (0.65 RFU) and directly on the beads (18 RFU). All images (16-bit) were acquired with 100 ms exposure time and minimum/maximum pixel intensities were adjusted for visualization purposes. RFU correspond to the grey scale intensity (0 to 65 536) divided by 1000.



effectively captured within the pores of the NBNM beads, contrarily to the longer LAMP products, thus generating a linear and directly proportional correlation between bead fluorescence and RNA copies with Ct ranging from 25 to 36 ($R^2 = 0.99$) (Fig. S1†). Schematics illustrating the bead capture behavior in the presence of LAMP or PCR positive and negative samples are shown as ESI† (Fig. S2).

Aiming at bringing cost-effective, rapid and sensitive COVID-19 diagnostics to RLS, the main goal of this work was to develop a robust but minimally complex and portable platform for SARS-CoV-2 RNA detection directly from heat inactivated biological samples. Taking advantage of the signal enhancement strategy reported in section 3.1. The concept was based on designing a PMMA disc with 20 independent channels (Fig. 2A) each comprising (1) a region to perform LAMP of 10 μ L sample (LAMP section), (2) a section containing packed NBNM beads at the interface between 400 and 50 μ m deep channels and (3) an outlet chamber (OC) connected to the previous two components *via* the narrow 50 μ m deep section. To process the sample added to the disc, the sequence of steps schematized in Fig. 2B was followed. The heat-inactivated swab sample containing template RNA was mixed with the LAMP reagents and a total of 10 μ L of the mixture was added to the channel, the access holes were sealed and the whole disc incubated at 65 $^{\circ}$ C. After amplification, the disc was subjected to four cycles of ramping the rotation linearly from 0 to 6000 rpm and *vice-versa* (1 cycle meaning 0–6000–0 rpm). During the ramp-up, the liquid is forced through the beads due to the centrifugal force and held back by an increase in pressure inside the sealed OC. During ramp-down, the decrease in centrifugal force allows the OC to decompress pushing the liquid backwards, while the denser agarose beads are still held in place by the centrifugal force. This back-and-forth motion with 4 cycles allows a complete capture of the primers in solution according to the previous results in Fig. 1B.

The portable platform developed to combine the centrifugal and heating modules required to perform the LAMP followed by the bead-based signal enhancement is shown in Fig. 3. The top centrifugal module shown in Fig. 3A uses a DC motor controlled by a microcontroller board and a hall-effect sensor to complete the rotation protocol. After the rotation protocol, the measurement is performed through a PMMA lens in the cover lid covered on the backside with a 100 μm polyimide film which is aligned with the smartphone camera with a custom-made adapter. The polyimide film serves as an emission absorption filter to block the excitation light from the 450 nm 80 mW laser embedded on the platform.⁵⁰ The laser diode is aligned at an angle of $\sim 17.5^\circ$ relative to the disc (Fig. S5†) to take advantage of total internal reflection of the PMMA–air interface between the



Fig. 2 Schematics and working principle of the on-disc LAMP fluorescence signal readout with bead-based signal enhancement. **A** – PMMA disc comprising 20 parallel channels packed with dried NBNM agarose beads. The disc is fabricated with 3 layers, a bottom (**B**) 1 mm PMMA layer with embedded 400 μm deep channels, a middle (**M**) layer comprising patterned double-sided PSA defining a 50 μm deep sieving channel preventing the flow of beads into the outlet chamber (**OC**), and a top (**T**) 1 mm PMMA layer with inlet and outlet access holes. **B** – Sequential operation of the disc after adding 10 μL of sample. The sequence comprises the (1) sealing of the inlet and outlet holes, (2) LAMP by heating the disc at 65 $^{\circ}\text{C}$ for 30 minutes, (3) ramping up the rotation speed to 6000 rpm to force the solution through the packed beads, followed by a ramp down to 0 rpm, resulting in a backflow of the liquid due to the pressure difference between the OC (positive pressure) and the LAMP region (negative pressure). The final two steps can be repeated multiple times to ensure complete capture of the target molecules in solution.

disc and the lens to minimize residual leakage of blue light into the camera sensor.

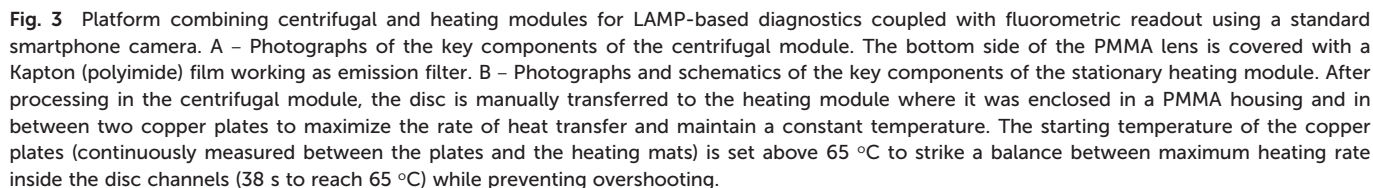
The heating module assembled below the centrifugal platform is shown in Fig. 3B. This module comprises a PMMA housing with a removable front piece to insert the disc. The disc enclosed by the housing is sandwiched in contact with two copper plates which are actively heated by two resistive silicone mats. The temperature control is achieved with a feedback loop measuring the temperature between the copper plates and the heating mats on both sides of the stack. The PMMA housing and the insulating foam on each side of the heating mats serves to minimize convective and conductive heat dissipation. To minimize non-specific amplification of hybridized primer dimer and primer-template pairs at lower temperatures, rapid heating is achieved by initially setting the temperature of the copper plates at 79 $^{\circ}\text{C}$ according to the plot in Fig. 3B. The plates are passively cooled down by the disc and active heating is only actuated once the temperature of the plates decreases below 65 $^{\circ}\text{C}$.

3.3. Characterization of the integrated platform and data acquisition

The developed platform was subsequently characterized by testing a dilution series of ORF1ab RNA fragment spiked in DI-water (Fig. 4). A dilution series using the complete

platform was tested and the results in Fig. 4A show a limit of detection between 10^2 – 10^3 copies per reaction (0% positive at 10^2 copies and 100% positive for 10^3 copies performing 4 independent measurements for each concentration). The analysis of the signal in each channel was performed by measuring the grayscale intensity profile of the green channel (average of 30 pixels) 100 pixels along the interface of the beads and the solution. Centering the 30×100 pixels line profile at the bead–solution interface (negative pixel values –50 to 0 in solution and positive values 0 to 50 on the beads), the response was described as a 10 pixel moving average relative to the intensity of the solution. A negative/positive decision threshold was defined according to 3.29 times the standard deviation of the relative signal obtained at the end of the line profile (pixel 50) for 5 independent negative controls (0.01% probability of false positive below the threshold). The obtained sensitivity for the on-disc LAMP was lower than that obtained in the RT-LAMP tests (Fig. 1A), where 100% of the samples with 10^2 /copies per reaction showed a positive signal. The relatively lower sensitivity is hypothesized to arise from non-specific adsorption of enzymes and/or template to the PMMA channel, having a significantly higher surface area in contact with the 10 μL of solution compared to a standard reaction tube. Efforts to improve channel passivation strategies or application of alternative materials are envisioned to maximize





obtained with initial RNA template titers as high as 10^9 copies per reaction. However, for this feature to be used without risk of false-positives, the processing of the disc post-heating has to be performed immediately at $t = 30$ min. Overall these results confirm the triple functionality of the agarose beads for (1) signal intensity enhancement, (2) sample preparation to remove non-specific background and (3) simple reaction inactivation at room temperature.

The developed platform was tested for the detection of SARS-CoV-2 viral RNA directly from nasopharyngeal swab samples collected in viral transport media resorting to a simple heat inactivation step (95 °C, 15 min). A set of 31 clinical samples



Fig. 4 Characterization of on-disc signal generation after on-disc LAMP. **A** – Relative grayscale intensity (green channel) measured at the interface between the solution and beads (50 pixels each side) performing the LAMP in the presence of increasing copy numbers of SARS-CoV-2 RNA fragment. The threshold value was calculated as the average difference between signal magnitude of the beads and solution minus 3.29 times the standard deviation of 5 independent negative measurements. Differences in signal magnitude at pixel 50 above and below the threshold are considered negative and positive, respectively. **B** – Enhancement of signal-to-noise ratio in solution provided by the NBNM beads. All images (green channel only) were acquired using a smartphone camera combined with illumination provided by the 450 nm laser diode and polyimide film as emission filter. **C** – Bead-based LAMP inactivation. The LAMP was performed on the disc after first flowing the mix through the NBNM beads according to the same rotation protocol used for the measurements.

(Table S1†) spanning Ct values from 11 to 27, including 6 negative controls, was initially tested using the conditions optimized above (Fig. S6†). It was observed that the iLACO primers are highly prone to false-positive results at 30 min of amplification time required to maximize sensitivity. To improve the assay performance, the alternative primer set developed by Rabe and Cepko⁴² (As1e), minimizing primer dimer amplification according to previous reports,⁴³ was tested and directly compared with the iLACO primer set for the amplification of full-length SARS-CoV-2 synthetic RNA (GenBank MN908947.3) spiked in water. The results of RT-LAMP shown in Fig. 5A highlight two critical improvements in assay performance. Firstly, non-specific amplification of primer dimers starts occurring only after 40 min of amplification time, a positive shift of more than 10 min relative to the iLACO primers. Secondly, lower RNA titers are amplified more rapidly with a loss in quantitative resolution, suggesting that a higher sensitivity can be achieved for the clinical samples keeping the amplification time constant at

30 min. However, despite the lower degree of non-specific amplification, the As1e primers result in an equally high background fluorescence signal resulting in positive to negative signal ratio of only 1.6-fold when measured on the disc at room temperature without the bead-based enhancement (Fig. S7†). Remarkably, NBNM agarose beads increase the positive to negative signal ratio more than 10 times up to approximately 17-fold (Fig. S7†).

The As1e primer set was subsequently used to test a wider panel of 131 nasopharyngeal swab samples (Table S1†) using RT-LAMP and the integrated platform in parallel. The results from the integrated platform were classified as (1) positive, (2) negative or (3) inconclusive according to the criteria detailed in Fig. S8†, highlighting a significant improvement in positive-negative result discrimination. The compiled results correlating the output of each LAMP assay with the Ct values of each sample and the time to positivity of RT-LAMP are shown in Fig. 5B (representative smartphone images shown as ESI† Fig. S9). In both assays, all samples with Ct





Fig. 5 Optimization of primer set, estimation of sensitivity/specificity and benchmarking of the integrated platform with an expanded panel of heat-inactivated nasopharyngeal swab samples. **A** – Comparison iLACO and As1e primers with RT-LAMP (benchtop thermocycler) in the presence of increasing copies of full-length synthetic SARS-CoV-2 RNA (GenBank MN908947.3) spiked in water. **B** – RT-LAMP and on-disc LAMP measurements of 131 heat inactivated nasopharyngeal swab samples (96 samples with Ct values ranging from 15.7 to 43.45 and 35 RT-PCR negative samples) using the As1e primer set. Ct values were measured in a Cepheid GeneXpert system and are the average of E and N genes. Each symbol in the top plot corresponds to a technical replicate of each sample. Color codes (all plots) and symbol shapes (bottom plots) correspond to different Ct value ranges according to the legend of Fig. 5. The abbreviations “Neg”, “Inc” and “Pos” refer to negative, inconclusive or positive result using the integrated platform. **C** – Sensitivity and specificity for the RT-LAMP (benchtop thermocycler) and LAMP-disc (on-disc LAMP using the integrated platform) measurements. The plotted mean values and Clopper-Pearson 95% confidence intervals were calculated using MedCalc software (Ostend, Belgium) diagnostic test evaluation calculator. RT-LAMP (1) and (2) refer to the sensitivity determined for two technical replicates. To determine the specificity, only the PCR negative samples were considered ($n = 35$). Filled and dashed boxes refer to RT-LAMP and LAMP-disc measurements, respectively.

values below 25 ($n = 23$) resulted in a positive response, while all samples with Ct values above 30 ($n = 77$) resulted in a negative response. Comparing the output of the RT-LAMP and the integrated platform, deviations in positive, inconclusive or negative outcomes were observed only for samples with Ct values between 25 and 30 around the detection limit of the assay. The sensitivity for high ($Ct < 26$) and low ($30 > Ct > 26$) viral titers and overall specificity was then calculated for each replicate of the RT-LAMP and for the integrated platform according to Fig. 5C. The performance of the integrated platform was comparable to the RT-LAMP performed on a benchtop thermocycler for the same samples, resulting in a sensitivity of 96.6% (82.2–99.9%, 95% CI) and a specificity of 100% (90–100%, 95% CI) for samples with Ct values < 26 . In both cases the sensitivity dropped significantly for Ct values > 26 . While LAMP has been reported to provide high sensitivity at higher Ct values in the

range of 25–30 for COVID-19 diagnostics, such performance can only be achieved with complex RNA extraction or sample clean-up procedures, which were not used in this case.^{40,51} Furthermore, considering that Ct values for RT-PCR vary significantly between laboratories (as much as 5 Ct for the 30–35 range),⁵² it was not possible to accurately quantify the absolute sensitivity of the developed platform for unprocessed clinical samples. Nevertheless, a Ct value of 26 using Cepheid GeneXpert corresponds broadly to a range of 1×10^4 – 1×10^5 copies per mL in transport medium according to previous reports using spiked samples.⁵²

4. Conclusions

We introduce a novel portable bead-based centrifugal microfluidic platform and demonstrate LAMP-based viral RNA detection directly from heat-inactivated nasopharyngeal



- 14 R. Wolfel, V. M. Corman, W. Guggemos, M. Seilmaier, S. Zange, M. A. Muller, D. Niemeyer, T. C. Jones, P. Vollmar, C. Rothe, M. Hoelscher, T. Bleicker, S. Brunink, J. Schneider, R. Ehmann, K. Zwirgmaier, C. Drosten and C. Wendtner, *Nature*, 2020, **581**, 465–469.
- 15 J. J. A. V. Kampe, D. A. M. C. van de Vijver, P. L. A. Fraaij, B. L. Haagmans, M. M. Lamers, N. Okba, J. P. C. van den Akker, H. Endeman, D. A. M. P. J. Gommers, J. J. Cornelissen, R. A. S. Hoek, M. M. V. der Eerden, D. A. Hesselink, H. J. Metselaar, A. Verbon, J. E. M. D. Steenwinkel, G. I. Aron, E. C. M. V. Gorp, S. V. Boheemen, J. C. Voermans, C. A. B. Boucher, R. Molenkamp, M. P. G. Koopmans, C. Geurtsvankessel and A. A. V. D. Eijk, *Nat. Commun.*, 2021, **12**, 267, DOI: 10.1101/2020.06.08.20125310.
- 16 M. J. Mina, R. Parker and D. B. Larremore, *N. Engl. J. Med.*, 2020, **383**, e120, DOI: 10.1056/NEJMp2025631.
- 17 J. Dinnes, J. J. Deeks, A. Adriano, S. Berhane, C. Davenport, S. Ditttrich, D. Emperador, Y. Takwoingi, J. Cunningham, S. Beese, J. Dretzke, L. Ferrante di Ruffano, I. M. Harris, M. J. Price, S. Taylor-Phillips, L. Hooft, M. M. Leeflang, R. Spijker, A. Van den Bruel and Cochrane COVID-19 Diagnostic Test Accuracy Group, *Cochrane Database Syst. Rev.*, 2020, **8**, CD013705.
- 18 A. Kalk and A. Schultz, *Lancet Infect. Dis.*, 2020, **20**, 1370, DOI: 10.1016/s1473-3099(20)30563-6.
- 19 H. Zhang, Y. Xu, Z. Fohlerova, H. Chang, C. Iliescu and P. Neuzil, *Trends Analyt. Chem.*, 2019, **113**, 44–53.
- 20 S. J. Oh, B. H. Park, J. H. Jung, G. Choi, D. C. Lee, D. H. Kim and T. S. Seo, *Biosens. Bioelectron.*, 2016, **75**, 293–300.
- 21 B. H. Park, S. J. Oh, J. H. Jung, G. Choi, J. H. Seo, D. H. Kim, E. Y. Lee and T. S. Seo, *Biosens. Bioelectron.*, 2017, **91**, 334–340.
- 22 H. Yan, Y. Zhu, Y. Zhang, L. Wang, J. Chen, Y. Lu, Y. Xu and W. Xing, *Sci. Rep.*, 2017, **7**, 1460.
- 23 A. A. Sayad, F. Ibrahim, S. M. Uddin, K. X. Pei, M. S. Mohktar, M. Madou and K. L. Thong, *Sens. Actuators, B*, 2016, **227**, 600–609.
- 24 D. Liu, Y. Zhu, N. Li, Y. Lu, J. Cheng and Y. Xu, *Sens. Actuators, B*, 2020, **310**, 127834.
- 25 F. Tian, C. Liu, J. Deng, Z. Han, L. Zhang, Q. Chen and J. Sun, *Sci. China: Chem.*, 2020, 1–9, DOI: 10.1007/s11426-020-9800-6.
- 26 E. S. Yamanaka, L. A. Tortajada-Genaro, N. Pastor and A. Maquieira, *Biosens. Bioelectron.*, 2018, **109**, 177–183.
- 27 H. Wang, Z. Ma, J. Qin, Z. Shen, Q. Liu, X. Chen, H. Wang, Z. An, W. Liu and M. Li, *Biosens. Bioelectron.*, 2019, **126**, 373–380.
- 28 L. Wan, J. Gao, T. Chen, C. Dong, H. Li, Y. Z. Wen, Z. R. Lun, Y. Jia, P. I. Mak and R. P. Martins, *Biomed. Microdevices*, 2019, **21**, 9.
- 29 K. R. Jackson, T. Layne, D. A. Dent, A. Tsuei, J. Li, D. M. Haverstick and J. P. Landers, *Forensic Sci. Int.: Genet.*, 2020, **45**, 102195.
- 30 J. Hui, Y. Gu, Y. Zhu, Y. Chen, S. J. Guo, S. C. Tao, Y. Zhang and P. Liu, *Lab Chip*, 2018, **18**, 2854–2864.
- 31 S. Wang, N. Liu, L. Zheng, G. Cai and J. Lin, *Lab Chip*, 2020, **20**, 2296–2305.
- 32 K. Kaarj, P. Akarapipad and J. Y. Yoon, *Sci. Rep.*, 2018, **8**, 12438.
- 33 S.-C. Liao, J. Peng, M. G. Mauk, S. Awasthi, J. Song, H. Friedman, H. H. Bau and C. Liu, *Sens. Actuators, B*, 2016, **229**, 232–238.
- 34 L. Yu, S. Wu, X. Hao, X. Dong, L. Mao, V. Pelechano, W.-H. Chen and X. Yin, *Clin. Chem.*, 2020, **66**, 975–977.
- 35 C. Yan, J. Cui, L. Huang, B. Du, L. Chen, G. Xue, S. Li, W. Zhang, L. Zhao, Y. Sun, H. Yao, N. Li, H. Zhao, Y. Feng, S. Liu, Q. Zhang, D. Liu and J. Yuan, *Clin. Microbiol. Infect.*, 2020, **26**, 773–779.
- 36 Y. H. Baek, J. Um, K. J. C. Antigua, J. H. Park, Y. Kim, S. Oh, Y. I. Kim, W. S. Choi, S. G. Kim, J. H. Jeong, B. S. Chin, H. D. G. Nicolas, J. Y. Ahn, K. S. Shin, Y. K. Choi, J. S. Park and M. S. Song, *Emerging Microbes Infect.*, 2020, **9**, 998–1007.
- 37 G. S. Park, K. Ku, S. H. Baek, S. J. Kim, S. I. Kim, B. T. Kim and J. S. Maeng, *J. Mol. Diagn.*, 2020, **22**, 729–735.
- 38 W. E. Huang, B. Lim, C. C. Hsu, D. Xiong, W. Wu, Y. Yu, H. Jia, Y. Wang, Y. Zeng, M. Ji, H. Chang, X. Zhang, H. Wang and Z. Cui, *Microb. Biotechnol.*, 2020, **13**, 950–961.
- 39 L. E. Lamb, S. N. Bartolone, E. Ward and M. B. Chancellor, *PLoS One*, 2020, **15**, e0234682.
- 40 V. L. D. Thi, K. Herbst, K. Boerner, M. Meurer, L. P. Kremer, D. Kirrmaier, A. Freistaedter, D. Papagiannidis, C. Galmozzi, M. L. Stanifer, S. Boulant, S. Klein, P. Chlanda, D. Khalid, I. B. Miranda, P. Schnitzler, H.-G. Kräusslich, M. Knop and S. Anders, *Sci. Transl. Med.*, 2020, **12**, eabc7075.
- 41 I. F. Pinto, C. R. F. Caneira, R. R. G. Soares, N. Madaboosi, M. R. Aires-Barros, J. P. Conde, A. M. Azevedo and V. Chu, *Methods*, 2017, **116**, 112–124.
- 42 B. A. Rabe and C. Cepko, *Proc. Natl. Acad. Sci. U. S. A.*, 2020, **117**, 24450–24458.
- 43 A. Alekseenko, D. Barrett, Y. Pareja-Sanchez, R. J. Howard, E. Strandback, H. Ampah-Korsah, U. Rovsniak, S. Zuniga-Veliz, A. Klenov, J. Malloo, S. Ye, X. Liu, B. Reinius, S. J. Elsassner, T. Nyman, G. Sandh, X. Yin and V. Pelechano, *Sci. Rep.*, 2021, **11**, 1820.
- 44 P. Novo, V. Chu and J. P. Conde, *Lab Chip*, 2014, **14**, 1991–1995.
- 45 R. J. Meagher, A. Priye, Y. K. Light, C. Huang and E. Wang, *Analyst*, 2018, **143**, 1924–1933.
- 46 C. S. Ball, Y. K. Light, C. Y. Koh, S. S. Wheeler, L. L. Coffey and R. J. Meagher, *Anal. Chem.*, 2016, **88**, 3562–3568.
- 47 L. Becherer, N. Borst, M. Bakheit, S. Frischmann, R. Zengerle and F. von Stetten, *Anal. Methods*, 2020, **12**, 717–746.
- 48 I. F. Pinto, M. R. Aires-Barros and A. M. Azevedo, *Pharm. Bioprocess.*, 2015, **3**, 263–279.
- 49 T. Matos, J. A. Queiroz and L. Bülow, *J. Mol. Recognit.*, 2014, **27**, 184–189.
- 50 S. Carturan, A. Quaranta, M. Bonafini, A. Vomiero, G. Maggioni, G. Mattei, C. de Julián Fernández, M. Bersani, P. Mazzoldi and G. Della Mea, *Eur. Phys. J. D*, 2007, **42**, 243–251.
- 51 V. L. Fowler, B. Armson, J. L. Gonzales, E. L. Wise, E. L. A. Howson, Z. Vincent-Mistiaen, S. Fouch, C. J. Maltby, S. Grippon, S. Munro, L. Jones, T. Holmes, C. Tillyer, J. Elwell, A. Sowood, O. de Peyer, S. Dixon, T. Hatcher, H. Patrick, S. Laxman, C. Walsh, M. Andreou, N. Morant, D. Clark, N.



- Moore, R. Houghton, N. J. Cortes and S. P. Kidd, *J. Infect.*, 2021, **82**, 117–125.
- 52 F. Wolters, J. van de Bovenkamp, B. van den Bosch, S. van den Brink, M. Broeders, N. H. Chung, B. Favie, G. Goderski, J. Kuijpers, I. Overvest, J. Rahamat-Langedoen, L. Wijsman, W. J. Melchers and A. Meijer, *J. Clin. Virol.*, 2020, **128**, 104426.
- 53 A. Ganguli, A. Mostafa, J. Berger, M. Y. Aydin, F. Sun, S. A. S. Ramirez, E. Valera, B. T. Cunningham, W. P. King and R. Bashir, *Proc. Natl. Acad. Sci. U. S. A.*, 2020, **117**, 22727–22735.
- 54 M. P. McRae, G. W. Simmons, N. J. Christodoulides, Z. Lu, S. K. Kang, D. Fenyo, T. Alcorn, I. P. Dapkins, I. Sharif, D. Vurmaz, S. S. Modak, K. Srinivasan, S. Warhadpande, R. Shrivastav and J. T. McDevitt, *Lab Chip*, 2020, **20**, 2075–2085.

